

Supporting Information

Origin of ferroelectricity in two prototypical hybrid organic-inorganic perovskites

Kai Li,^{¶,†} Zhi-Gang Li,^{¶,†} Jun Xu,[†] Yan Qin,[†] Wei Li,^{*,†} Alessandro Stroppa,[‡] Keith T. Butler,^{*,§} Christopher J. Howard,^{||} Martin T. Dove,[⊥] Anthony K. Cheetham,[#] and Xian-He Bu^{*,†}

[†]School of Materials Science and Engineering & Tianjin Key Laboratory of Metal and Molecule-Based Material Chemistry, Nankai University, Tianjin 300350, China

[‡] CNR-SPIN, c/o Dip. to di Scienze Fisiche e Chimiche, Università degli Studi dell'Aquila, Via Vetoio, 67100 Coppito (AQ), Italy

[§]Department of Chemistry, University of Reading, Reading, RG6 6AD, UK

^{||} School of Engineering, University of Newcastle, New South Wales 2308, Australia

[⊥] College of Computer Science, Sichuan University, Chengdu, Sichuan 610065, China

[#]Department of Materials Science and Metallurgy, University of Cambridge, Cambridge CB3 0FS, UK

[¶]These authors contributed equally to this work.

Table S1 Crystal data and structure refinement.

	[(DMA)[Mn(N ₃) ₃]		[DMA][Mn(HCOO) ₃]
<i>T</i> /K	240	300	293
Formula	C ₂ H ₈ MnN ₁₀	C ₂ H ₈ MnN ₁₀	C ₅ H ₁₁ MnNO ₆
<i>M_w</i>	227.12	227.12	236.08
Crystal system	monoclinic	monoclinic	trigonal
Space group	<i>P</i> 2 ₁	<i>P</i> 2 ₁ / <i>n</i>	<i>R</i> $\bar{3}$ <i>c</i>
<i>a</i> (Å)	6.2152(12)	8.6503(4)	8.3261(3)
<i>b</i> (Å)	10.0630(2)	12.2018(7)	8.3261(3)
<i>c</i> (Å)	7.1647(14)	8.6541(4)	22.8793(8)
α (°)	90	90	90
β (°)	93.62	90.50	90
γ (°)	90	90	120
<i>V</i> (Å ³)	447.21(15)	913.40(8)	1373.59(11)
<i>Z</i>	2	4	6
$\rho_{\text{calcd.}}$ / (g·cm ⁻³)	1.687	1.652	1.712
μ / mm ⁻¹	1.451	11.612	11.817
<i>F</i> (000)	230.0	460.0	726.0
<i>GOF</i>	1.138	1.087	1.155
<i>R</i> ₁ ^{<i>a</i>} [<i>I</i> > 2 <i>s</i> (<i>I</i>)]	<i>R</i> ₁ =0.0987, <i>wR</i> ₂ =0.2912	<i>R</i> ₁ =0.0657, <i>wR</i> ₂ =0.1753	<i>R</i> ₁ =0.0314, <i>wR</i> ₂ =0.0958
<i>wR</i> ₂ ^{<i>b</i>} (all data)	<i>R</i> ₁ =0.1079, <i>wR</i> ₂ =0.2946	<i>R</i> ₁ =0.0808, <i>wR</i> ₂ =0.1851	<i>R</i> ₁ =0.0351, <i>wR</i> ₂ =0.1000

$$a, R_1 = \sum ||F_o| - |F_c|| / \sum |F_o|; b, wR_2 = [\sum w(F_o^2 - F_c^2)^2 / \sum w(F_o^2)^2]^{1/2}.$$

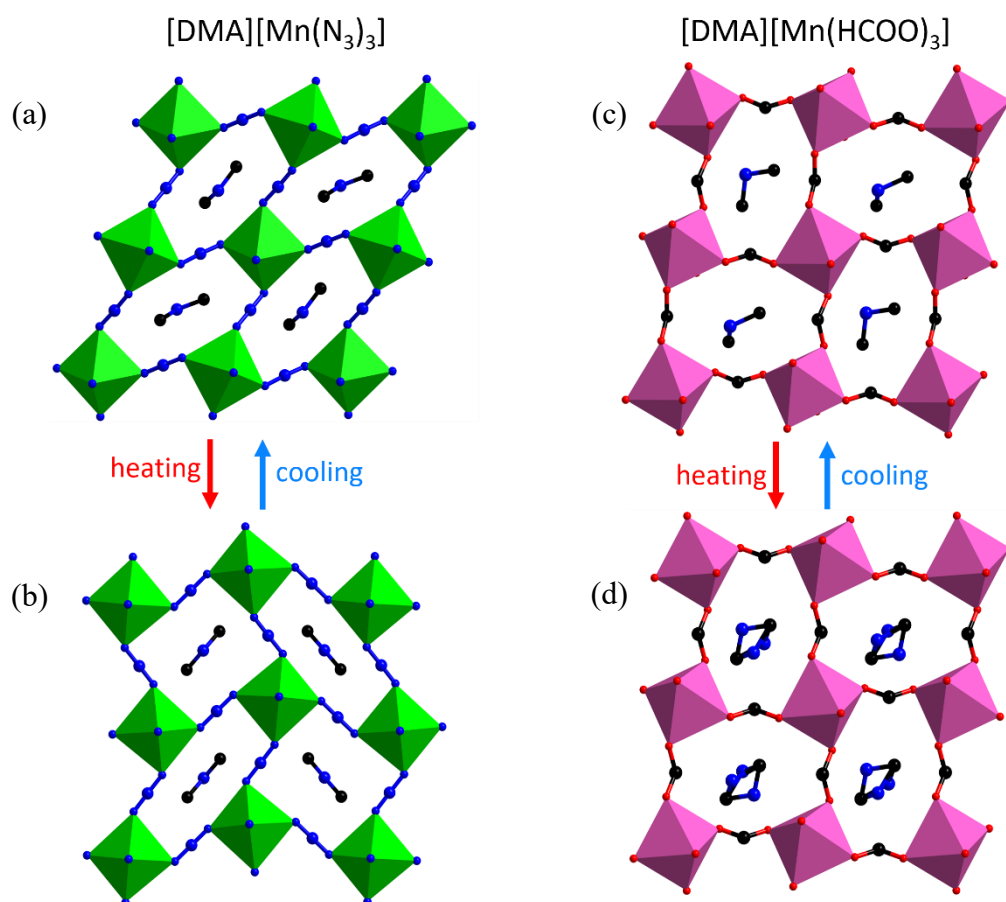


Figure S1 Crystal structures of the LT and HT phases of (a and b) $[\text{DMA}][\text{Mn}(\text{N}_3)_3]$ and (c and d) $[\text{DMA}][\text{Mn}(\text{HCOO})_3]$. All H atoms are omitted here for clarity. Color scheme: C, black; N, blue; O, red; Mn, green.

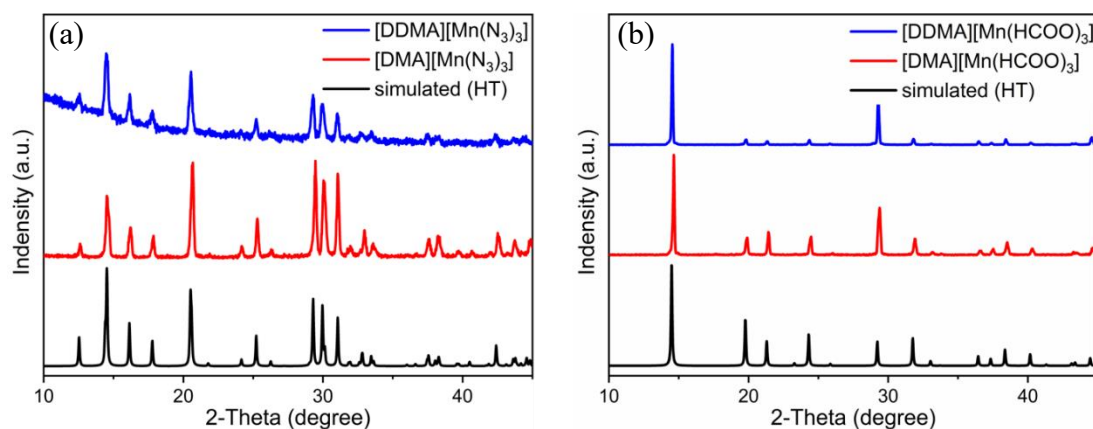


Figure S2 Experimental and simulated powder X-ray diffraction (PXRD) patterns of $[\text{DMA}][\text{Mn}(\text{N}_3)_3]$ and $[\text{DMA}][\text{Mn}(\text{HCOO})_3]$, verifying the purity of their ordinary and deuterated samples. The patterns of $[(\text{DMA})][\text{Mn}(\text{N}_3)_3]$ and $[(\text{DDMA})][\text{Mn}(\text{N}_3)_3]$ were measured at 333 and 373 K, respectively.

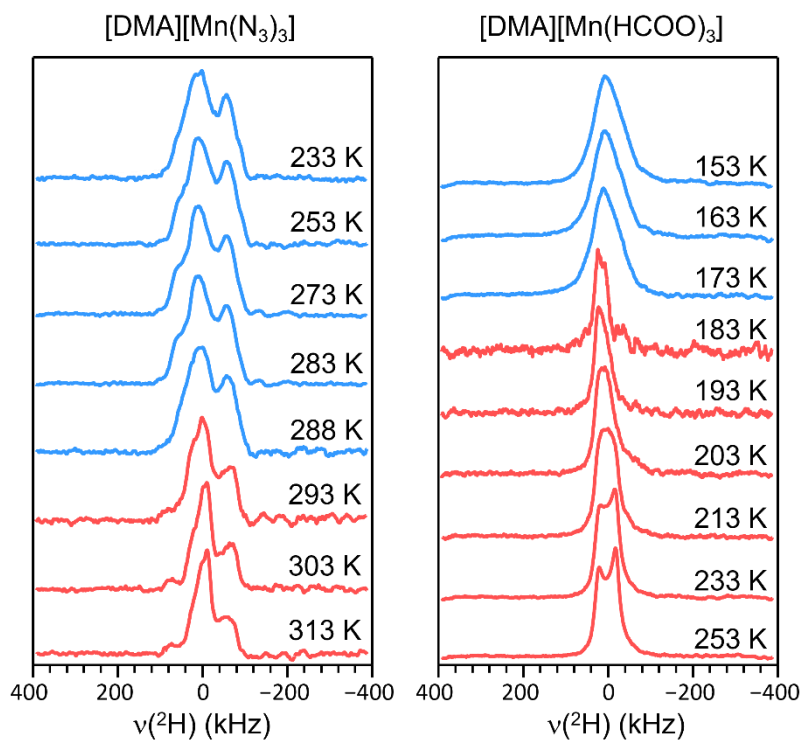


Figure S3 The variable-temperature ^2H solid-state NMR spectra at different temperatures of $[\text{DMA}][\text{Mn}(\text{N}_3)_3]$ and $[\text{DMA}][\text{Mn}(\text{HCOO})_3]$.

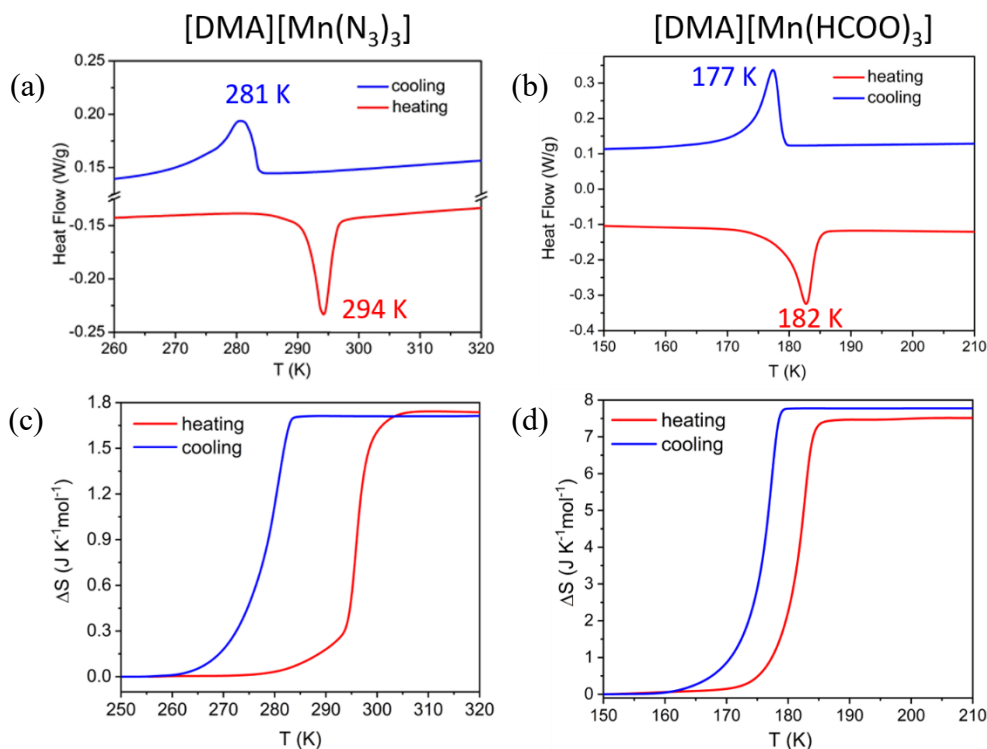


Figure S4 (a) DSC curves of [DMA][Mn(N₃)₃] and (b) [DMA][Mn(HCOO)₃] measured on both the heating and cooling runs. The entropy changes across phase transitions of (c) [DMA][Mn(N₃)₃] and (d) [DMA][Mn(HCOO)₃] were obtained by integrating the DSC curves of (a) and (b).

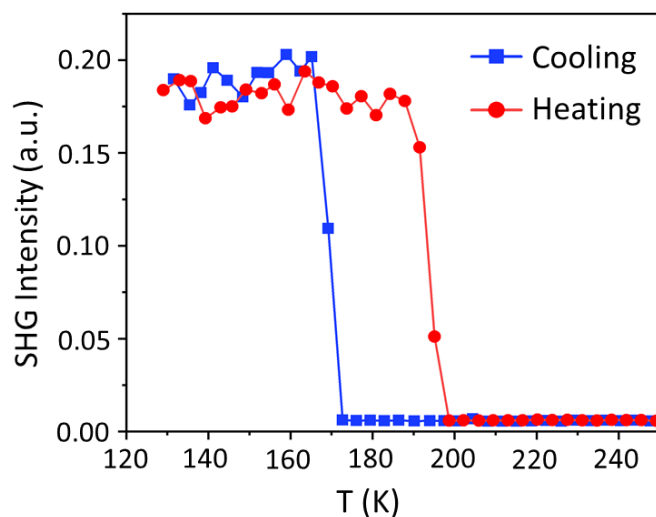


Figure S5 The temperature-dependent SHG responses obtained in both the heating and cooling runs of [DMA][Mn(HCOO)₃].

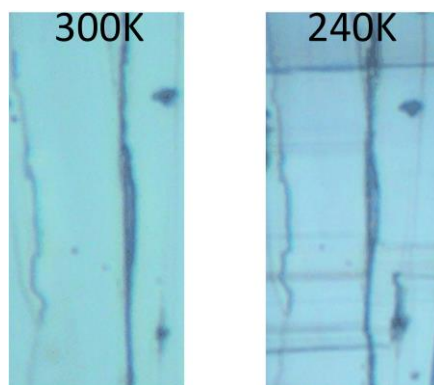


Figure S6 In-situ optical microscopical photographs of a block crystal of $[\text{DMA}][\text{Mn}(\text{N}_3)_3]$ at 240 and 300 K. It is obvious that the transverse cracks emerge at 240 K, indicating its single-crystal state has been destroyed.

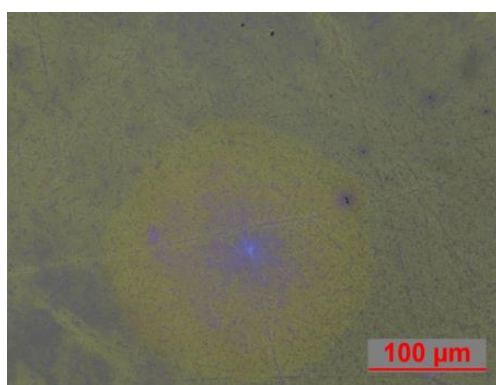


Figure S7 Optical microscopical photograph of the thin film of $[\text{DMA}][\text{Mn}(\text{N}_3)_3]$.

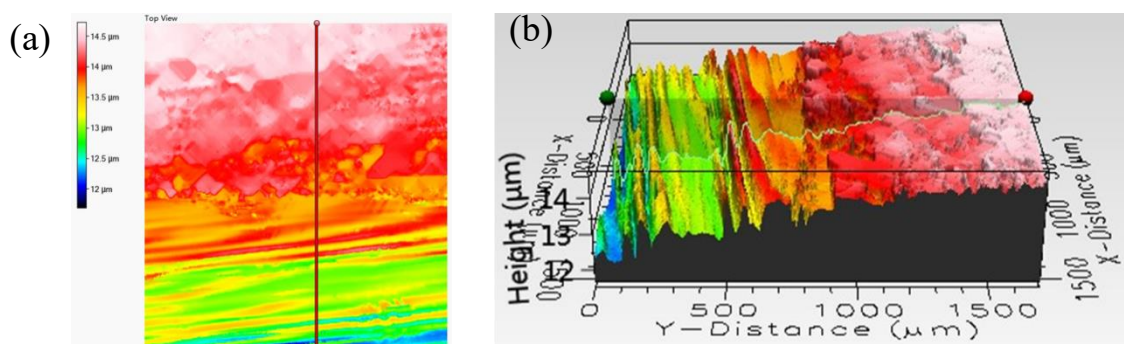


Figure S8 The characterization of thin-film contour and thickness measurement by step profile, the thickness of this thin-film is about 1.5 μm .

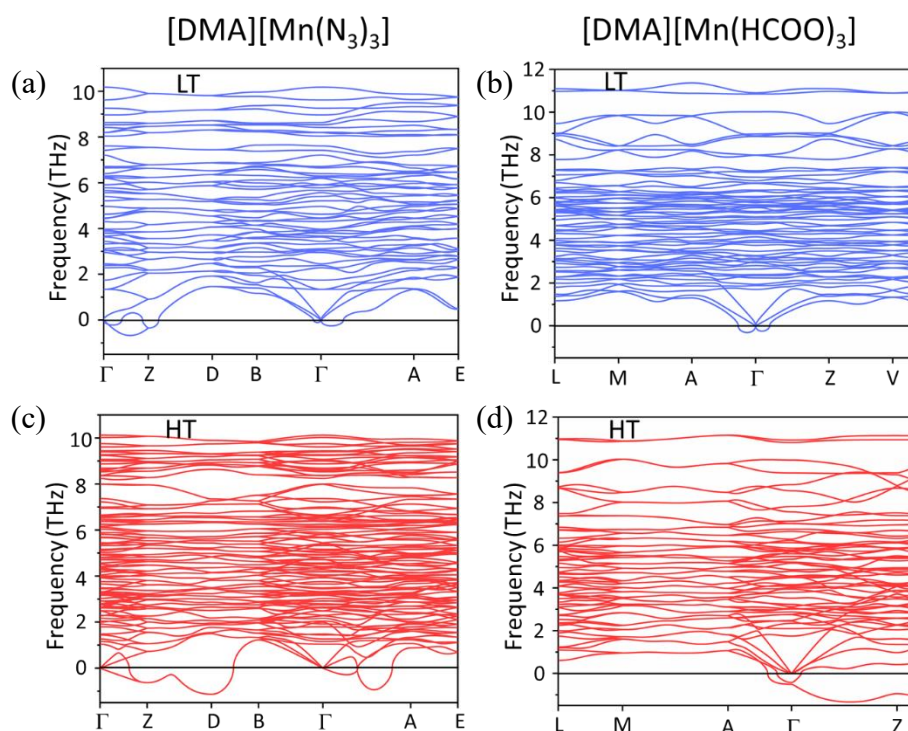


Figure S9 The calculated harmonic phonon dispersion of the LT and HT phases of (a and b) [DMA][Mn(N₃)₃] and (c and d) [DMA][Mn(HCOO)₃].

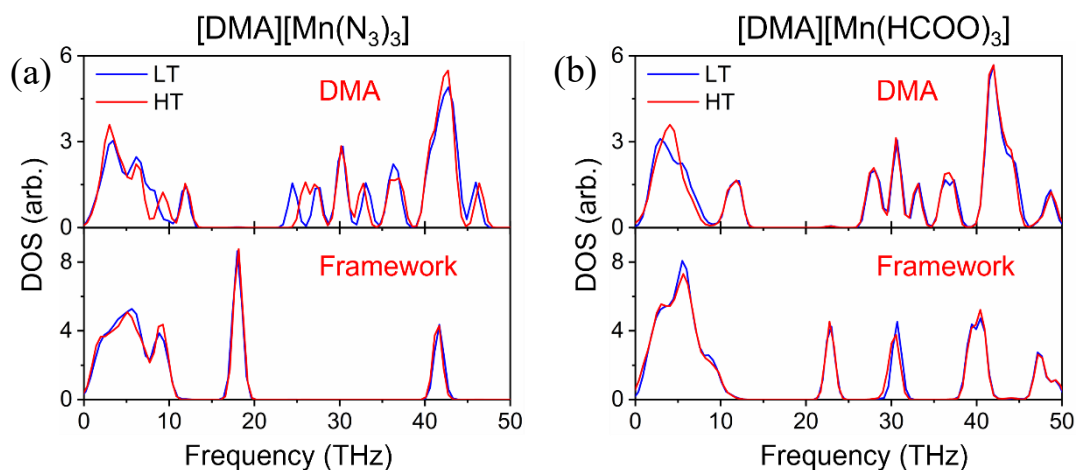


Figure S10 The partial phonon density of states for both HT and LT phases of [DMA][Mn(N₃)₃] (a) and [DMA][Mn(HCOO)₃] (b): the upper and bottom parts are DMA and the anionic framework contributions, respectively.

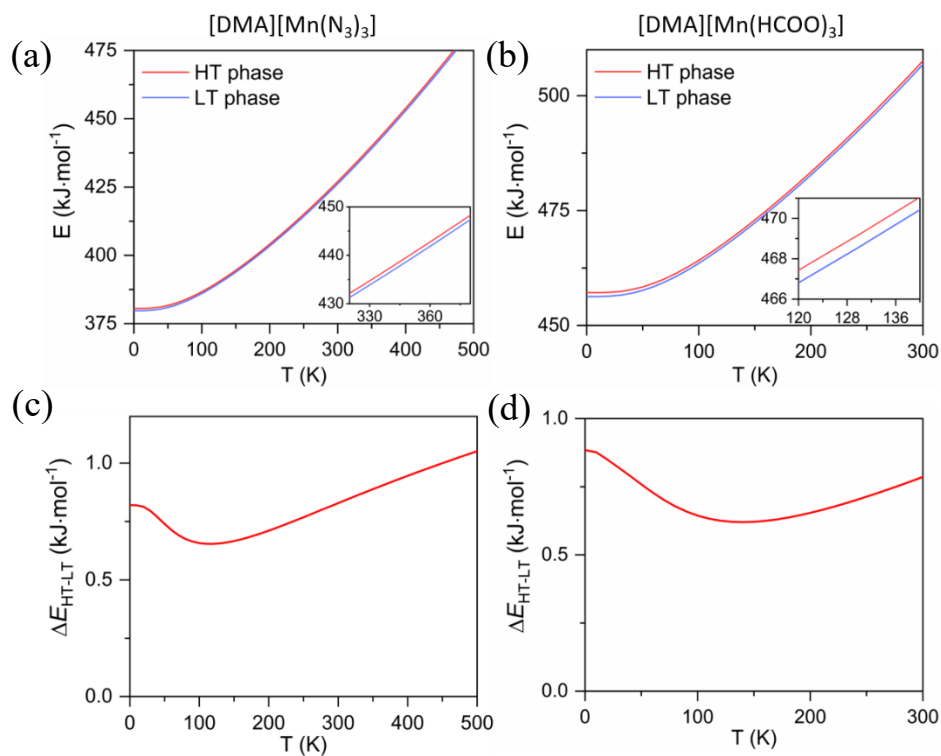


Figure S11 The change of vibrational energy in dependence of temperature for both HT and LT phases of the two perovskites (a and b) when imaginary frequency modes were excluded. The insets are their partial enlarged plots. The difference of vibrational energy between HT and LT of the two perovskites (c and d).

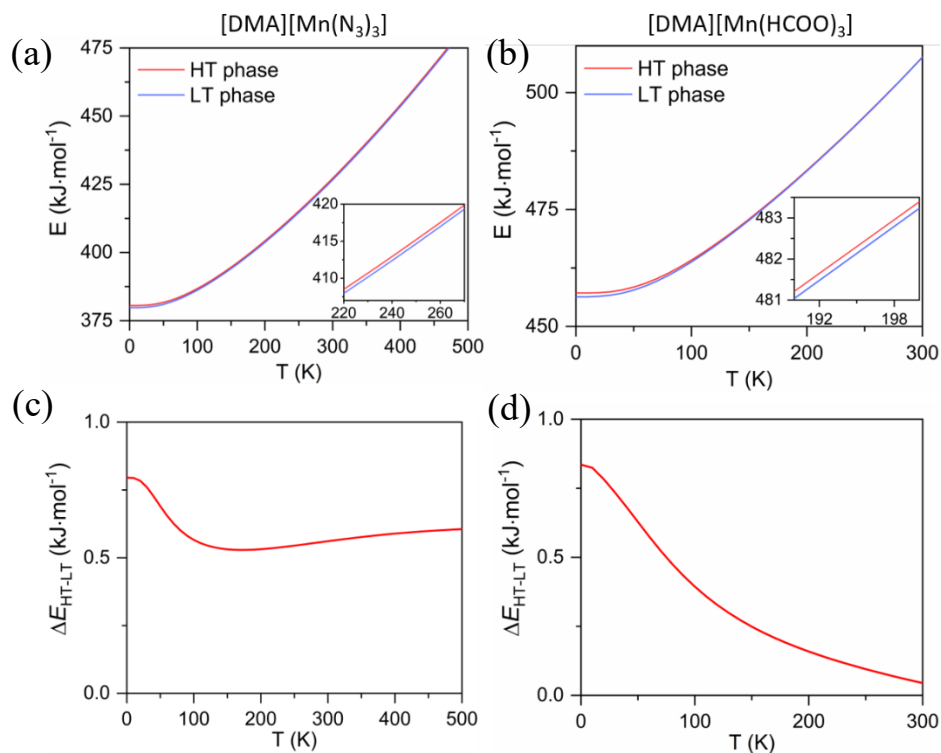


Figure S12 The change of vibrational energy in dependence of temperature for both the HT and LT phases of the two perovskites (a and b) when the imaginary frequency modes were included. The insets are their partial enlarged plots. The difference of vibrational energy between HT and LT of the two perovskites (c and d)

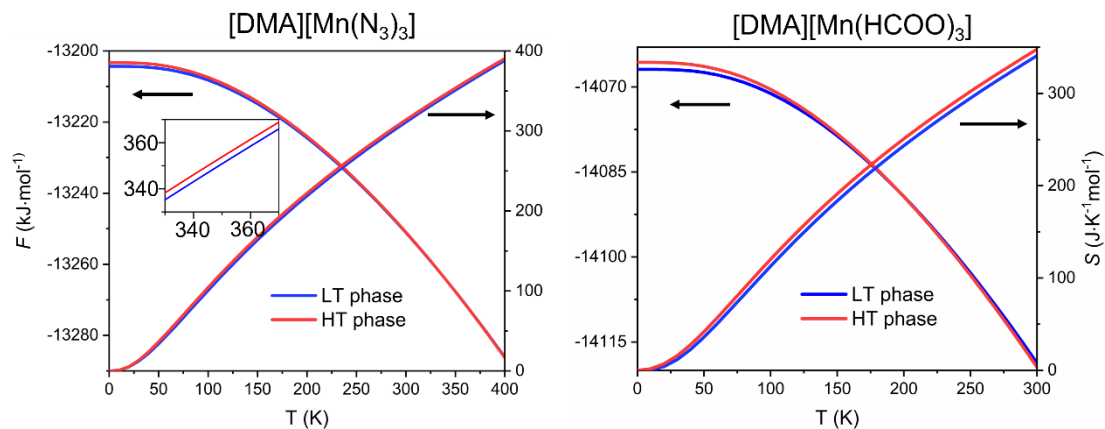


Figure S13 The change of free energy and vibrational entropy in dependence of temperature for both the HT and LT phases of the two perovskites when the imaginary frequency modes are excluded. The inset in the left figure is the partially enlarged plot in the region of 330-370 K.

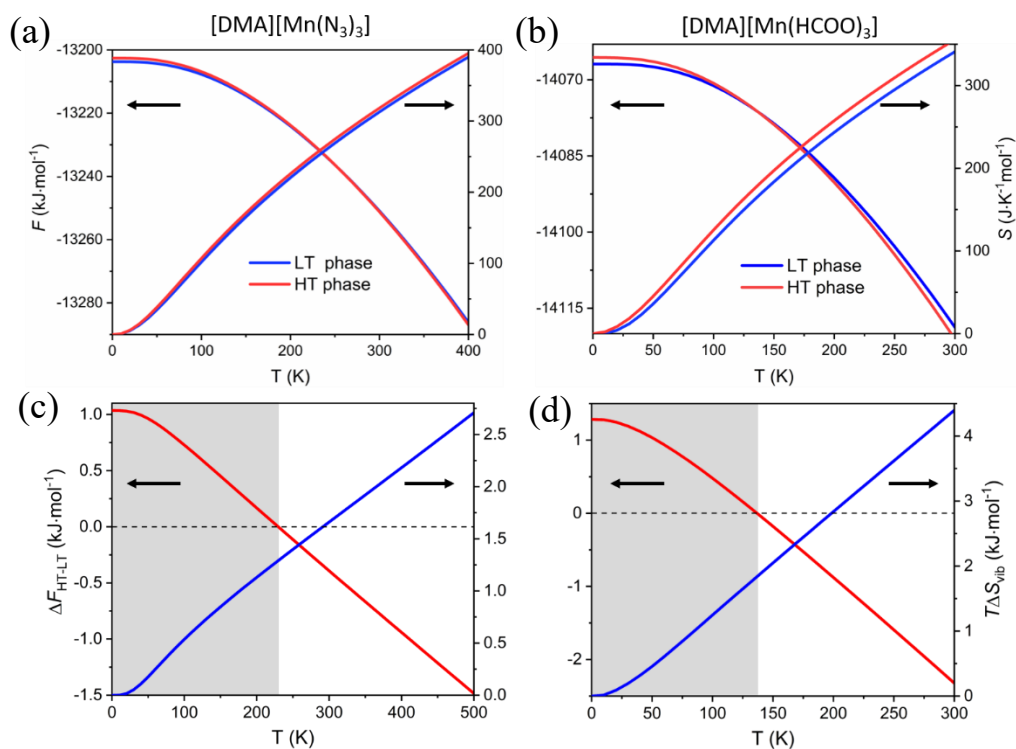


Figure S14 The calculated thermodynamic properties of (a and c) [DMA][Mn(N₃)₃] and (b and d) [DMA][Mn(HCOO)₃] as a function of temperature when the imaginary frequency modes are included.

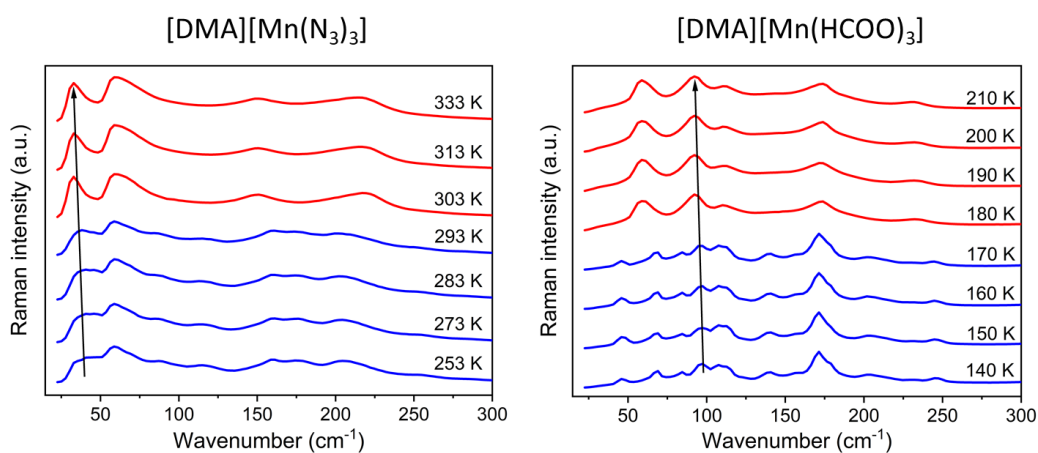


Figure S15 The temperature-dependent Raman spectra of [DMA][Mn(N₃)₃] and [DMA][Mn(HCOO)₃].

Note S1: Space group determination of [DMA][Mn(N₃)₃] HT phase

The reported space group of HT phase of [DMA][Mn(N₃)₃] is orthorhombic *Cmca*¹, however, we identify the HT structure to be in the monoclinic space group *P2₁/n*. The reasons are as follows:

Firstly, the powder X-ray diffraction patterns shown in Figure S18 for the HT phase of [DMA][Mn(N₃)₃] show that the *P2₁/n* space group gives an obviously better fitting than that of *Cmca* in the 2θ range of 30.5-34.0° and 37.0-39.0°.

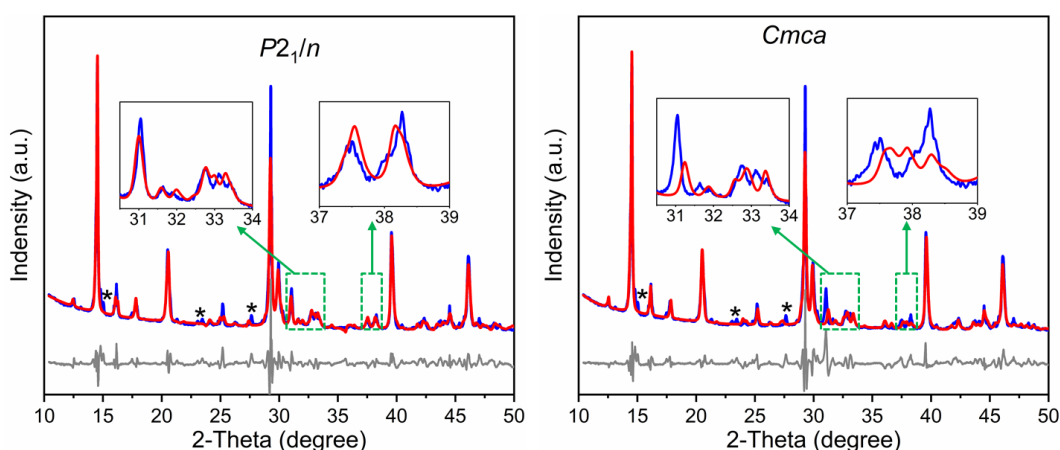


Figure S16 The Le-Bail refinements in the *P2₁/n* (left) and *Cmca* (right) space groups of the powder XRD patterns of [DMA][Mn(N₃)₃]. The insets are the partially enlarged plots in the 2θ range of 30.5-34.0° and 37.0-39.0°. The peaks marked by “*” belong to the LT phase.

Secondly, to further justify the symmetry of the HT phase of [DMA][Mn(N₃)₃], we have optimized both the *P2₁/n* and *Cmca* structures using DFT. The calculated results demonstrate that the low symmetry *P2₁/n* structure possesses lower energy (-141.2693 eV) compared with the high symmetry *Cmca* structure (-141.1882 eV).

Thirdly, the symmetry change across the ferroelectric phase transition of $[\text{DMA}][\text{Mn}(\text{N}_3)_3]$ would violate the Aizu notation² if the HT structure adopted the $Cmca$ space group. Accordingly, the HT structure of $[\text{DMA}][\text{Mn}(\text{N}_3)_3]$ is more reasonable to be in the $P2_1/n$ space group rather than $Cmca$.

Note S2: Group theoretical analysis

Group theoretical analysis has been applied to examine the distortions of the HT and LT frameworks of the two HOIPs relative to the framework in the notional cubic structure with space group $Pm\bar{3}m$, shown in Figure S16.³⁻⁵ Note that the DMA^+ cations were removed from the structures so that their frameworks could be compared with that of notional cubic parent directly. These comparisons were performed using ‘Method 4: Mode decomposition of a distorted structure’ in program ISODISTORT, analysis results as follows.

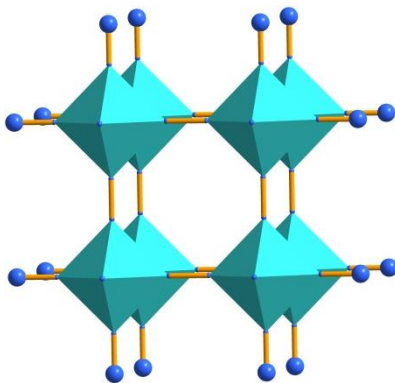


Figure S17 The notional cubic parent framework in space group $Pm\bar{3}m$.

$[\text{DMA}][\text{Mn}(\text{N}_3)_3]$: In the HT structure, there are significant distortions associated with a combination of irreducible representations (irreps) R_4^+ ($\mathbf{k} = \frac{1}{2}, \frac{1}{2}, \frac{1}{2}$), M_3^- ($\mathbf{k} = \frac{1}{2}, \frac{1}{2}, 0$), Γ_4^+ , and Γ_5^+ . $R_4^+(a,b,0)$ represents an out-of-phase tilting, Glazer symbol $a^-b^0c^-$,⁴

around the [100] and [001] axes of the HT monoclinic structure. $M_3^-(0,a,0)$ corresponds to columnar shifts along the [010] direction.⁶ In the LT structure, $M_3^-(0,0,a)$ is still there, representing a columnar shift along [100] direction. Irreps R_4^+ , I_4^+ , and I_5^+ have disappeared and new tilts M_3^+ and M_5^+ appear. $M_3^+(0,0,a)$ is an in-phase tilt, $a^+b^0c^0$, around monoclinic [100], while $M_5^+(0,0,0,0,a,a)$ is an unconventional tilt⁴ around monoclinic [001]. Note that the structure incorporates a ferroelectric distortion $I_4^-(0,a,-a)$ generating a dipole along [010] direction, which is the unique axis of the monoclinic. In summary, the HT structure could be generated from the notional cubic by a combination of irreps R_4^+ and M_3^- principally whereas the LT structure could be derived from a combination of tilt M_3^+ , columnar shift M_3^- , and ferroelectric displacement I_4^- .

[DMA][Mn(HCOO)₃]: The HT and LT structures correspond to entries #8 and #47 in Table 1 of reference.⁵ The distortions of HT structure only involve the out-of-phase tilting R_4^+ , $a^-a^-a^-$, which is ascribed to its high symmetry structure. In its LT structure, a ferroelectric displacement I_4^- develops, while tilting R_4^+ , $a^-a^-c^-$, is maintained.

Note S3: Strain analysis of [DMA][Mn(N₃)₃]

With respect to the monoclinic to monoclinic phase transition, the values of the strain of [DMA][Mn(N₃)₃] are given by

$$\begin{aligned} e_1 &= \frac{a}{a_0} - 1 \\ e_2 &= \frac{b}{b_0} - 1 \\ e_3 &= \frac{c \sin \beta}{c_0 \sin \beta_0} - 1 \end{aligned}$$

$$e_5 = \frac{c \cos \beta}{c_0 \sin \beta_0} - \frac{a \cos \beta_0}{a_0 \sin \beta_0}$$

$$e_4 = e_6 = 0$$

in which $a = \sqrt{2}a'$, $b = \sqrt{\sqrt{2}b'}$, $c = \sqrt{\sqrt{2}c'}$. Here, a' , b' , c' and β are lattice parameters of the LT structure, and a_0 , b_0 , c_0 , and β_0 are the lattice parameters of the HT structure.⁷ Substituting crystal data into formulae, the obtained strain values are as followed.

Table S2 The calculated strain parameters of $[\text{DMA}][\text{Mn}(\text{N}_3)_3]$ across its ferroelectric phase transition.

e_1	e_2	e_3	e_4	e_5	e_6
0.016	-0.019	-0.018	0	0.062	0

Across the phase transition, the linear strain components e_1 , e_2 and e_3 are ~ 1.6 , -1.9 and -1.8% , respectively, giving a total volume strain ($\approx e_1 + e_2 + e_3$) of $\sim 2.1\%$. However, the shear strain e_5 has a remarkably large value of $\sim 6.2\%$, which is comparable to the shear strains of ~ 5 - 10% in Jahn-Teller type perovskites.^{8,9}

Note S4: Calculation of polarization according to a point charge model

$[\text{DMA}][\text{Mn}(\text{N}_3)_3]$:

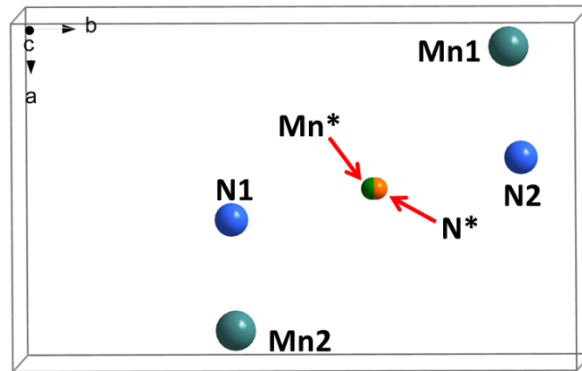


Figure S18 Distribution of Mn and N (in DMA⁺) atoms of [DMA][Mn(N₃)₃] in a unit cell (ferroelectric phase). Mn* and N* are the positive and negative centers.

Based on the point charge model, we assume that the centers of the positive charges of the DMA⁺ and the negative charges of the [Mn(N₃)₃][−] are located on the N atoms and Mn atoms, respectively. In a unit cell of the LT phase at 240 K, two N atoms and two Mn atoms are located at (0.5760, 0.3830, 0.7657), (0.4240, 0.8830, 0.2343) and (0.0804, 0.8758, 0.7520), (0.9196, 0.3758, 0.2408), respectively. Thus, the centers of the positive (Mn*) and negative (N*) ions are located at (0.5000, 0.6258, 0.5000) and (0.5000, 0.6330, 0.5000), respectively. A remnant electric dipole moment (P_s) appears along the b axis with a value of 4.29 $\mu\text{C}/\text{cm}^2$.

$$P_s = [(-e \times 0.6258) \times 2 + (e \times 0.6330) \times 2] \times c / V = (1.92 \times 10^{-29} \times \text{C} \times \text{m}) / (447.21 \times 10^{-30} \text{m}^3) = 4.29 \mu\text{C}/\text{cm}^2$$

Note S5: The influence of imaginary modes on results

To investigate the influence of imaginary modes for the results, the vibrational entropy and free energy with included imaginary mode contributions of the two HOIPs were estimated. The results with the inclusion of the imaginary modes indicate that the phase transition temperatures are 230 and 137 K with the vibrational entropy changes of 5.519 and 13.432 J·K^{−1}·mol^{−1} for [DMA][Mn(N₃)₃] and [DMA][Mn(HCOO)₃], respectively (Figure S14). Compared with the transition temperatures (342 and 196 K) and the vibrational entropy changes (2.964 and 7.492 J·K^{−1}·mol^{−1}) of the two HOIPs

when the negative modes are not considered, there is some difference. However, the conclusion, that the vibrational entropy differences drive these ferroelectric phase transitions, stays the same. We note that the inclusion or exclusion of the negative modes in the calculations of thermodynamic properties is not strictly physical, so the reported results in the main article are those excluding negative modes.

Reference

1. Zhao, X.-H.; Huang, X.-C.; Zhang, S.-L.; Shao, D.; Wei, H.-Y.; Wang, X.-Y., Cation-dependent magnetic ordering and room-temperature bistability in azido-bridged perovskite-type compounds. *J. Am. Chem. Soc.* **2013**, *135* (43), 16006-16009.
2. Aizu, K., Possible species of ferroelastic crystals and of simultaneously ferroelectric and ferroelastic crystals. *J. Phys. Soc. Jpn.* **1969**, *27* (2), 387-396.
3. Howard, C. J.; Stokes, H. T., Group-theoretical analysis of octahedral tilting in perovskites. *Acta Crystallogr. Sect. B* **1998**, *54* (6), 782-789.
4. Glazer, A., The classification of tilted octahedra in perovskites. *Acta Crystallogr. Sect. B* **1972**, *28* (11), 3384-3392.
5. Stokes, H. T.; Kisi, E. H.; Hatch, D. M.; Howard, C. J., Group-theoretical analysis of octahedral tilting in ferroelectric perovskites. *Acta Crystallogr. Sect. B* **2002**, *58* (6), 934-938.
6. Boström, H. L. B., Tilts and shifts in molecular perovskites. *CrystEngComm* **2020**, *22* (5), 961-968.
7. Carpenter, M. A.; Salje, E. K. H.; Graeme-Barber, A., Spontaneous strain as a determinant of thermodynamic properties for phase transitions in minerals. *Eur. J. Mineral.* **1998**, *10* (4), 621-691.
8. Li, W.; Zhang, Z.; Bithell, E. G.; Batsanov, A. S.; Barton, P. T.; Saines, P. J.; Jain, P. K.; Howard, C. J.; Carpenter, M. A.; Cheetham, A. K., Ferroelasticity in a metal–organic framework perovskite; towards a new class of multiferroics. *Acta Mater.* **2013**, *61* (13), 4928-4938.
9. Carpenter, M. A.; Meyer, H.; Sondergeld, P.; Marion, S.; Knight, K. S., Spontaneous strain variations through the low temperature phase transitions of deuterated lawsonite. *Am. Mineral.* **2003**, *88* (4), 534-546.